Pumping Flow in a Channel With a Peristaltic Wall

Yeng-Yung Tsui[1]
Professor
e-mail: yytsui@mail.nctu.edu.tw

Da-Ching Guo

Shin-Hung Chen

Shi-Wen Lin

Department of Mechanical Engineering,
National Chiao Tung University,
Hsinchu 300, Taiwan

Simplified models were widely used for analysis of peristaltic transport caused by contraction and expansion of an extensible tube. Each of these models has its own assumptions, and therefore, weakness. To get rid of the limitations imposed by the assumptions, a numerical procedure is employed to simulate this pumping flow in the present study. In earlier studies, the frame of reference adopted moves with the peristaltic speed of the vibrating wall so that the flow becomes steady. The flow characteristics in a wavelength were the main concern. In our calculations, a channel of finite length with a flexible wall is considered. Pressures are prescribed at the inlet and outlet boundaries. The computational grid is allowed to move according to the oscillation of the wall. Another state-of-the-art technique employed is to construct the grid in an unstructured manner to deal with the variable geometry of the duct. The effects of dimensionless parameters, such as amplitude ratio, wave number, Reynolds number, and back pressure on the pumping performance are examined. Details of the peristaltic flow structure are revealed. Also conducted is the comparison of numerical results with the theoretical predictions obtained from the lubrication model to determine the suitability of this theory. [DOI: 10.1115/1.4026077]

1 Introduction

Peristalsis is a form of pumping transport by means of progressive waves propagating along the flexible wall of a channel. Physiologically, it is a phenomenon of muscle contraction/expansion to move the contents within muscular tubes. It is responsible for the vasomotion of small blood vessels, urine flow from kidney to bladder, chyme movement in the gastro-intestinal tract, ovum movement in the fallopian tube, among others. This principle has been realized in industries to develop roller and finger pumps for transport of materials, such as foods, slurries, corrosive fluids, etc. to prevent them from being in contact to the mechanical parts of the pump. Especially in biomedical applications, it is desired not to cause drastic changes in the properties of the fluid being handled because blood, proteins, enzymes, etc., are sensitive to the shear rates. Peristaltic flow is preferred owing to its lower shear stresses.

For analysis of fluid mechanics involved in the peristaltic transport, simplified mathematical models have been proposed. Shapiro et al. [1] assumed that the wave length-to-channel height ratio is infinite and the Reynolds number is so small that the flow becomes a creeping motion in a narrow duct. The problem can be further simplified by adopting a frame of reference moving at the speed of wave. The flow then becomes steady because the wavy wall is stationary in this frame. The results of their analysis showed that under certain conditions an internally circulating bolus of fluid, i.e., a phenomenon of trapping, was found in the centerline region and transported with the wave speed. The findings were confirmed by the experiments of Weinberg et al. [2]. This model then becomes the most widely adopted of the methods used for analysis of this kind of flow.

Mishra and Rao [3] examined the peristaltic flow in an asymmetric channel with the traveling waves of different phase and amplitude propagating along the walls. Hayat and Ali [4] extended the model to investigate the effect of variable viscosity. The influence of lateral walls on peristaltic flow was discussed by Reddy et al. [5]. Ravi Kumar et al. [6] employed the slip boundary condition to model the permeable wall. Heat transfer was considered by Srinivas and Kothandapani [7]. Bifurcations of streamline patterns in planar and axisymmetric peristaltic flows were investigated in the study of Jiménez-Lozano and Sen [8].

The flow of various fluids in medical, chemical, and biotechnological engineering shows a complex rheological behavior. In the case of blood, such phenomenon mainly owes to the presence of erythrocytes. In order to model this behavior, various non-Newtonian models were employed. In the study of Misra and Pandey [9], the peristaltic flow of blood in small vessels was investigated using a two-layer fluid model in which the core region of the channel is described by Casson fluid and the peripheral region is taken to be Newtonian. The peristalsis of blood motion in a tapered channel was under investigation by Misra and Maiti [10] in which blood was treated as a Herschel-Bulkley fluid. The flow of a power-low fluid in a porous tube was considered by Rao and Mishra [11] while a similar fluid flow in an asymmetric porous channel was considered by Ravi Kumar et al. [12]. The study of Nadeem et al. [13] was concerned with Carreau fluid flow in a rectangular duct. A study of pseudoplastic fluid flow was reported by Noreen et al. [14]. Micropolar fluid was the main concern of Ali and Hayat [15]. A generalized Burgers' model was employed by Tripathi [16] to model the viscoelastic property of fluid. By assigning different values to the material constants, it reduces to fractional Oldroyd-B, fractional Maxwell, and fractional second grade fluids, along with the Newtonian fluid.

Perturbation theory is an alternative for theoretical analysis which was adopted by Fung and Yih [17] and Yin and Fung [18]. In principle, this model is appropriate only for small wave amplitudes because it is based on series expansion in powers of amplitude-to-channel height ratio. No such restriction is required in the Shapiro's model. However, the nonlinear inertial effects are included to allow a finite value of Reynolds number. It was applied by Wilson and Panton [19] to investigate the flow caused by bending and contraction waves. Selverov and Stone [20] and Yi et al. [21] examined the flow in a closed cavity induced by small-amplitude traveling waves along the boundary. Abd Elnaby and Haroun [22] extended the theory to include a compliant wall. The effect of wall properties on the peristaltic flow was investigated. In the studies of Usha and Rao [23] and Rao and Mishra [24], the perturbation series was expanded in terms of channel height-to-wave length ratio to examine curvature effects on the flow in symmetric and asymmetric channels.

It is obvious that either of the two above approaches has its own inherent shortcomings. The lubrication model can only deal with small Reynolds numbers, very low-frequency oscillations,

[1]Corresponding author.

Contributed by the Fluids Engineering Division of ASME for publication in the JOURNAL OF FLUIDS ENGINEERING. Manuscript received October 4, 2012; final manuscript received October 10, 2013; published online December 18, 2013. Assoc. Editor: Zhongquan Charlie Zheng.

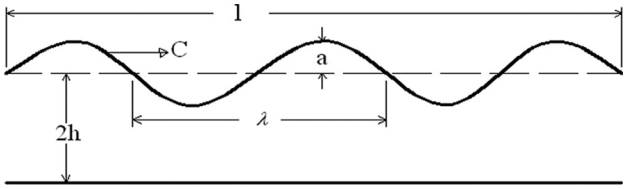

Fig. 1 Schematic sketch of the peristaltic channel

and long wavelengths whereas the perturbation theory is suitable only for small wall deformations and only asymptotic solutions are obtained. Another option for analysis is to solve the Navier-Stokes equations directly using computational fluid dynamics techniques. In these numerical calculations, it is essential to deal with the complex geometry of the channel wall, which contracts and expands in a traveling wave form. A usual way used in the past to simplify the problem is, first, to make a coordinate transformation from the laboratory frame to the wave frame so that the flow becomes steady. Orthogonal curvilinear coordinates were then used to fit the wavy wall in finite difference calculations in the study of Brown and Hung [25]. Takabatake and Ayukawa [26] introduced an oblique-lattice-coordinate technique into their difference schemes to tackle the irregular boundary. Finite element methods were adopted by Tong and Vawter [27] and Rathish Kumar and Naidu [28]. A boundary element method was used by Pozrikidis [29].

In the past decades, the finite volume method has emerged as an alternative to the finite element method to cope with irregular geometries encountered in fluid mechanics problems because unstructured grids can also be used. The main advantages of the former over the latter are that this kind of method is relatively easy to implement and the resulting difference equations can be solved efficiently using iterative methods because, like the finite difference method, the coefficient matrices have the sparse character. In the present study, a method based on the finite volume approach is introduced. Unlike the above simulations, the laboratory frame of reference is used and unsteady calculations are performed. To allow the computational domain to change in accordance with the wave propagation, governing equations are formulated in the Lagrangian-Eulerian form. The previous studies are mainly focused on the flow characteristics in steady state in one wavelength. We will evaluate the performance of the peristaltic pumping in a duct of finite length under certain pressure differences.

2 Mathematical Methods

A schematic drawing of the channel under consideration is shown in Fig. 1. It has a length l and a height $2h$. The lower wall is fixed while the upper wall moves in a sinusoidal form with amplitude a, wavelength λ, and speed c. The flexible wall can be expressed as

$$y_1(x,t) = 2h + a\cos\frac{2\pi}{\lambda}(x - ct) \tag{1}$$

The flow is regarded as incompressible and laminar due to the low wave speed. The computational grid is allowed to vary in accordance with the time varying geometry of the channel. The conservation equations for continuity and momentum can then be written in the following integral form as:

$$\frac{\partial}{\partial t}\int_\Omega \rho d\Omega + \int_S \rho\left(\vec{v} - \vec{v}_g\right)\cdot d\vec{S} = 0 \tag{2}$$

$$\frac{\partial}{\partial t}\int_\Omega \rho\vec{v}d\Omega + \int_S \rho\vec{v}\otimes\left(\vec{v} - \vec{v}_g\right)\cdot d\vec{S} = \int_S (\mu\nabla\vec{v})\cdot d\vec{S} - \int_\Omega \nabla p d\Omega \tag{3}$$

where ρ is the density, p is the pressure, μ is the viscosity, $\vec{v}$ is the fluid velocity, and $\vec{v}_g$ is the grid velocity. The grid, which moves in space, must also obey the conservation law [30],

$$\frac{\partial}{\partial t}\int_\Omega d\Omega - \int_S \vec{v}_g\cdot d\vec{S} = 0 \tag{4}$$

Multiplying the space conservation equation by ρ and subtracting it from Eq. (2) leads to the following form:

$$\int_S \rho\vec{v}\cdot d\vec{S} = 0 \tag{5}$$

which means that it is not necessary to consider the grid velocity in the continuity equation.

The above formulations are nondimensionalized using half the channel height h as the length scale and the wave speed c as the velocity scale. As an example, Eq. (1) can then be cast into the form,

$$y_1^*(x^*,t^*) = 2 + \varepsilon\cos 2\pi\alpha(x^* - t^*) \tag{6}$$

where $x^* = x/h$, $t^* = ct/h$, $\varepsilon = a/h$ are the amplitude ratio, and $\alpha = h/\lambda$ is the wave number.

A pressure based method within the frame of finite volume approach had been developed by the group of the present authors to deal with complex flows [31,32], including the case of the multichamber peristaltic micropump [33]. Therefore, only a brief introduction of the method is presented in the following.

The convective flux through the surface of the control volume can be approximated by

$$F^c = \sum_f \dot{m}_f^r\phi_f \tag{7}$$

Here the subscript f designates face value and the summation is over all the faces surrounding the control volume. The symbol ϕ represents each of the velocity components and ϕ_f is approximated by blending upwind and central difference schemes using the values at the two cell centroids adjacent to the considered face. The variable $\dot{m}_f^r$ is the mass flux relative to the moving face,

$$\dot{m}_f^r = \dot{m}_f - \frac{\rho\Delta\Omega_f}{\Delta t} \tag{8}$$

where $\Delta\Omega_f$ is the volume swept by the moving face and $\dot{m}_f$ is the mass flux based on flow velocities in the laboratory frame.

The diffusive flux crossing the control surface is approximated in the following way, suitable for unstructured grids of arbitrary topology:

$$F^d = \sum_f \left[\frac{\mu S_f^2}{\vec{\delta}_{PC}\cdot\vec{S}_f}(\phi_C - \phi_P) + \mu\overline{\nabla\phi}_f\left(\vec{S}_f - \frac{S_f^2}{\vec{\delta}_{PC}\cdot\vec{S}_f}\vec{\delta}_{PC}\right)\right] \tag{9}$$

Here $\vec{S}_f$ is the surface vector of the face f. The subscripts P and C denote the centroids of the principal and neighboring cells on the two sides of the considered face and $\vec{\delta}_{PC}$ is the distance vector directed from P to C (see Fig. 2). The face gradient $\overline{\nabla\phi}_f$ is obtained by linear interpolation from the gradient values at the two centroids.

After discretization, the momentum equation can be solved to find velocities using prevailing pressure field. However, the resulting velocity field does not obey the continuity law and the pressure needs to be updated. A pressure equation can be derived by adjusting the velocities in the way that the continuity equation (5) is satisfied. For conservation of mass in a cell the mass flux at

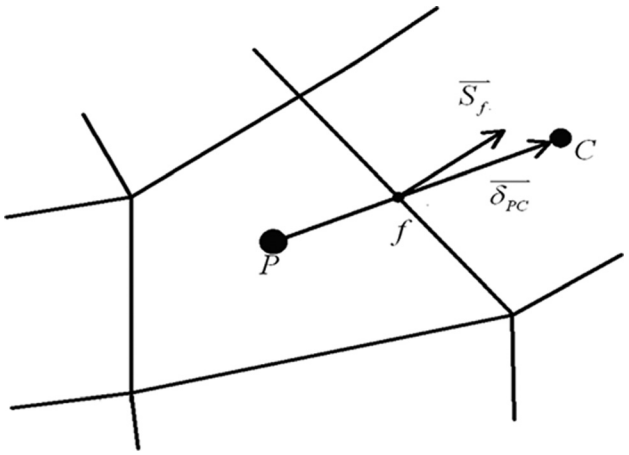

Fig. 2 Illustration of a typical control volume

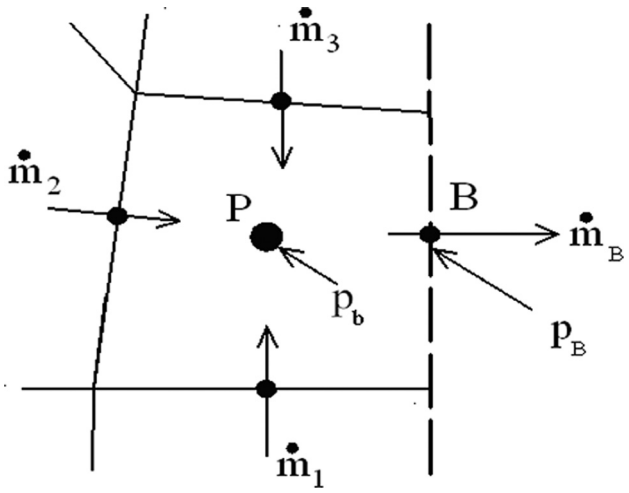

Fig. 3 A control volume adjacent to the open boundary

each face of the cell needs to be estimated, which is obtained using a momentum interpolation approach [31] as

$$\dot{m}_f = \rho_f \bar{\vec{v}}_f \cdot \vec{S}_f - B_f[(p_C - p_P) - \overline{\nabla p}_f \cdot \vec{\delta}_{PC}] \tag{10}$$

where the overbars denote the value obtained via interpolation from the two centroids P and C, and B_f denotes a coefficient. Details about the derivation of the pressure equation are given in Ref. [31].

The coupling between momentum and pressure equations can be treated in an iterative manner, similar to the SIMPLE algorithm, by solving these equations sequentially until convergence is reached in each time step. This iterative procedure is very time-consuming. As an alternative, the noniterative, predictor-corrector procedure of the PISO algorithm [34] is employed. After the momentum equations are solved, it is followed by two correction steps to adjust pressure and velocities. In the first corrector, the adjustment is similar to that of the SIMPLE algorithm. This procedure relies on the second corrector to make the pressure field to get rid of the mass residual left by the predictor step and to yield better approximation to the momentum conservation.

Pressures are specified at the inlet and outlet of the channel and flow flux through the channel must be sought. A method, based on mass conservation, is employed to fulfill this task. Figure 3 illustrates a cell P next to an open boundary B. Boundary pressure p_b is prescribed at the centroid of this cell. An extrapolation practice is undertaken to find the pressure on the boundary node. With this boundary face pressure p_B, the velocity at centroid P can be

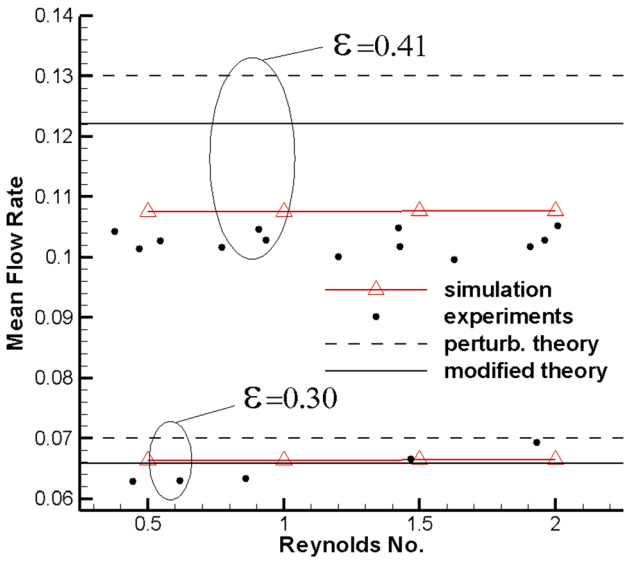

Fig. 4 Comparison with theoretical solutions and experiments for two amplitudes

obtained by solving momentum equation as described above. After mass fluxes through all internal faces are calculated using the momentum interpolation method given by Eq. (10), the mass flux through boundary face $\dot{m}_B$ is then obtained via conservation of mass,

$$\dot{m}_B = -\sum_{i \neq B} \dot{m}_i \tag{11}$$

where $\dot{m}_i$ denotes the mass flux through internal face and the summation is taken over all the internal faces.

3 Results and Discussion

The geometry under consideration has been given in Fig. 1. The dimensionless length of the channel is 32 and the width 2. The variables of the flow system can be grouped into four dimensionless parameters: amplitude ratio $\varepsilon = a/h$, wave number $\alpha = h/\lambda$, Reynolds number $\mathrm{Re} = \rho c h/\mu$, and dimensionless back pressure $P_b = p_b/\rho c^2$. It is noted that zero pressure is given at the inlet and the back pressure specified at the outlet represents the pressure difference across the entire channel.

Before examining the effects of the parameters, the accuracy of the computational procedure needs to be verified. Three different grids with 10×80, 20×160, and 40×320 cells are used for grid sensitivity test. For a case with amplitude ratio $\varepsilon = 0.3$, wave number $\alpha = 0.0907$, Reynolds number $\mathrm{Re} = 1$, and back pressure $P_b = 0$ the mean flow rates obtained for the three different grids are 0.06587, 0.06609, and 0.06632. Obviously, the results are not sensitive to the grids used in the calculations.

In calculations, the amplitude of the wave is increased gradually to its final value during the first period and the computation proceeds for several periods to reach periodic steady state. The mean flow rates at period numbers 2, 4, 6, and 8 are 0.6501, 0.8124, 0.8188, and 0.8191 for the case $\varepsilon = 1.0$, $\alpha = 0.3125$, $\mathrm{Re} = 20$, and $P_b = 0$. It can be seen that at least six periods of computation are required to obtain steady-state solutions.

Validation of the calculation is made in Fig. 4 by comparing the experiments of Yin and Fung [18] for the configuration $\alpha = 0.0907$, $P_b = 0$ and two different amplitude ratios $\varepsilon = 0.30$ and 0.41. It is obvious that the dimensionless mean flow rate $\bar{Q}(= Q/ch$, where Q represents the time-mean flow rate at each cross section) is independent of the Reynolds number which lies within a limited range of small values between 0.5 and 2. Also presented are the results obtained from the perturbation theory of Fung and

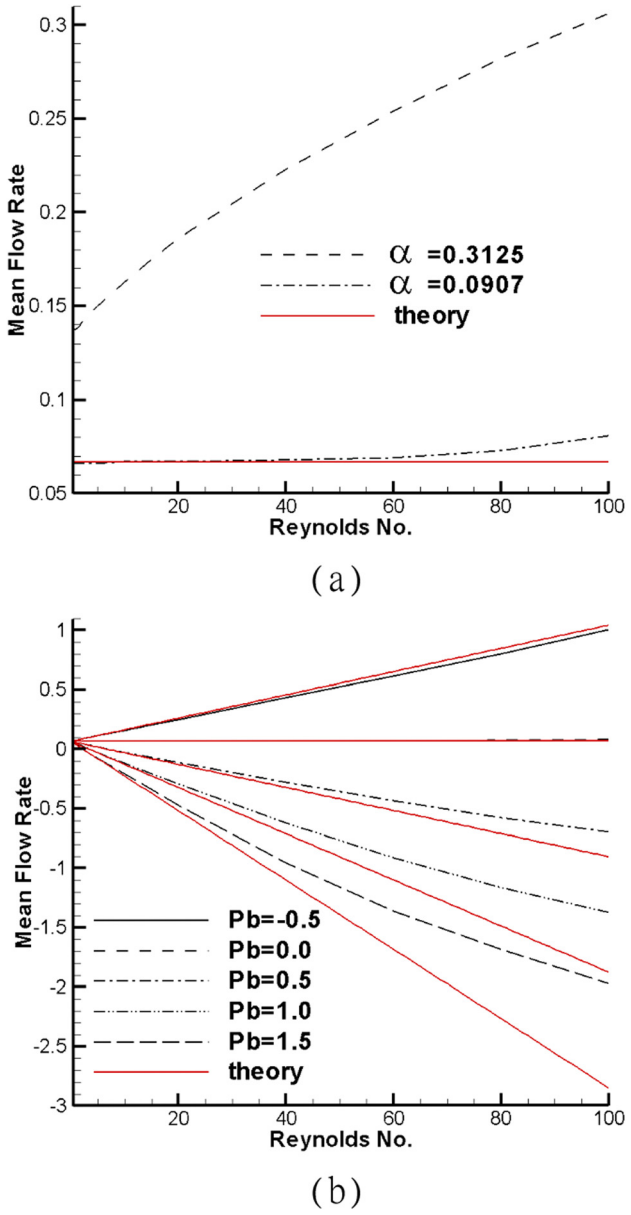

Fig. 5 Variation of mean flow rate against Reynolds number with $\varepsilon = 0.3$ for (*a*) two wave numbers ($P_b = 0$) and (*b*) different back pressures ($\alpha = 0.0907$)

Yih [17]. The curves marked by "modified theory" are obtained by taking account of the side effects of the three-dimensional channel in the theoretical results. The appearance of the side walls leads to higher viscous losses, and thus, lower fluid flows. For the larger amplitude case the numerical predictions perform better than the theoretical one even when the side wall effects are accounted for. The higher flow rates of the present calculations than the measured ones can be attributed to the 3D effects not included in simulations. For the smaller amplitude case the flow rate is lower and the results obtained by different methods are close.

Based on the above tests, confidence is acquired about the accuracy of the solution method. In the following, the effects of the four dimensionless parameters on the peristaltic pumping are examined individually. We will compare our calculations with the analytical solution obtained from the lubrication model of Shapiro et al. [1], which is briefly described in the Appendix. The resulting relation between dimensionless mean flow rate and dimensionless back pressure is given by

$$\bar{Q} = 2 - \frac{4(4-\varepsilon^2)}{(8+\varepsilon^2)} - \frac{\mathrm{Re}}{6}\frac{(4-\varepsilon^2)^{5/2}}{(8+\varepsilon^2)}\frac{P_b}{L} \tag{12}$$

where $L(= l/h)$ represents dimensionless length of the channel. It can be found that maximum flow ($\bar{Q} = 2$) is yielded when the channel is completely occluded ($\varepsilon = 2$) and no net flow is induced ($\bar{Q} = 0$) when there is no driving pressure force ($P_b = 0$) and peristalsis ($\varepsilon = 0$).

3.1 Effects of Reynolds Number. Figure 5(*a*) presents the variation of mean flow rate against Reynolds number for amplitude ratio $\varepsilon = 0.3$ and back pressure $P_b = 0$. The Reynolds number is varied in the range up to 100. Two wave numbers are considered. For the low wave number case ($\alpha = 0.0907$) the mean flow rate remains nearly as a constant, being seen in Fig. 4. As the wave number is enlarged to 0.3125, the flow rate is greatly increased and becomes an increasing function of Reynolds number. The analytic solution obtained from Eq. (12) is also shown in the figure. It is noted from the equation that the mean flow rate depends on amplitude ratio only when the back pressure is zero. The numerical solution for the low wave number case agrees well with the theoretical solution except at high Reynolds numbers close to 100. Based on the understanding that, as will be stressed later, the lubrication theory is valid only when the wave number is small, it is not surprising to find significant differences between the numerical results for the large wave number case and the theoretical one.

Given by Eq. (12), a linear relationship exists between flow rate and Reynolds number. It becomes an increasing function for negative P_b and a decreasing function for positive P_b, as identified in Fig. 5(*b*) (for $\alpha = 0.0907$). The lubrication theory is appropriate only for small Reynolds numbers. Thus, it is not surprising that the discrepancy between numerical predictions and analytical solutions increases with Reynolds number, which is especially true for the condition of adverse pressure gradient. In general, the relation between mean flow rate and Reynolds number becomes nonlinear when the Reynolds number is greater than 20. Equation (12) also shows that the flow rate becomes a function of amplitude ratio only at zero Reynolds number. At this limit, $\bar{Q} = 0.067$ for $\varepsilon = 0.3$. Thus, all curves are directed toward this point in the figure as Reynolds number approaches zero.

3.2 Effects of Amplitude Ratio. The effects of amplitude ratio on mean flow rate for the case of zero back pressure and wave number $\alpha = 0.0907$ are illustrated in Fig. 6(*a*). Under the condition of zero pressure gradients, Eq. (12) can be reduced to

$$(\bar{Q})_{P_b=0} = 2 - \frac{4(4-\varepsilon^2)}{(8+\varepsilon^2)} \tag{13}$$

It is seen from Fig. 6(*a*) that this equation is valid for the Reynolds numbers up to 20. Figure 6(*b*) presents the results for back pressures −0.5, 0, and 1.5. At low amplitudes, the flow in the channel is mainly driven by the pressure gradient. As a consequence, the differences between these different back pressure cases are significant at low values of amplitude. However, the differences dwindle as ε increases because the amplitude effect gradually becomes more important. When the channel is completely occluded ($\varepsilon = 2$), $\bar{Q} = 2$. This is the reason why all the curves tend to merge at high amplitudes.

3.3 Effects of Wave Number. The lubrication theory of Shapiro et al. assumes that the peristaltic wavelength is very large, and thus the wave number must be very small. This leads to the results that the flow rate is independent of wave number, as seen

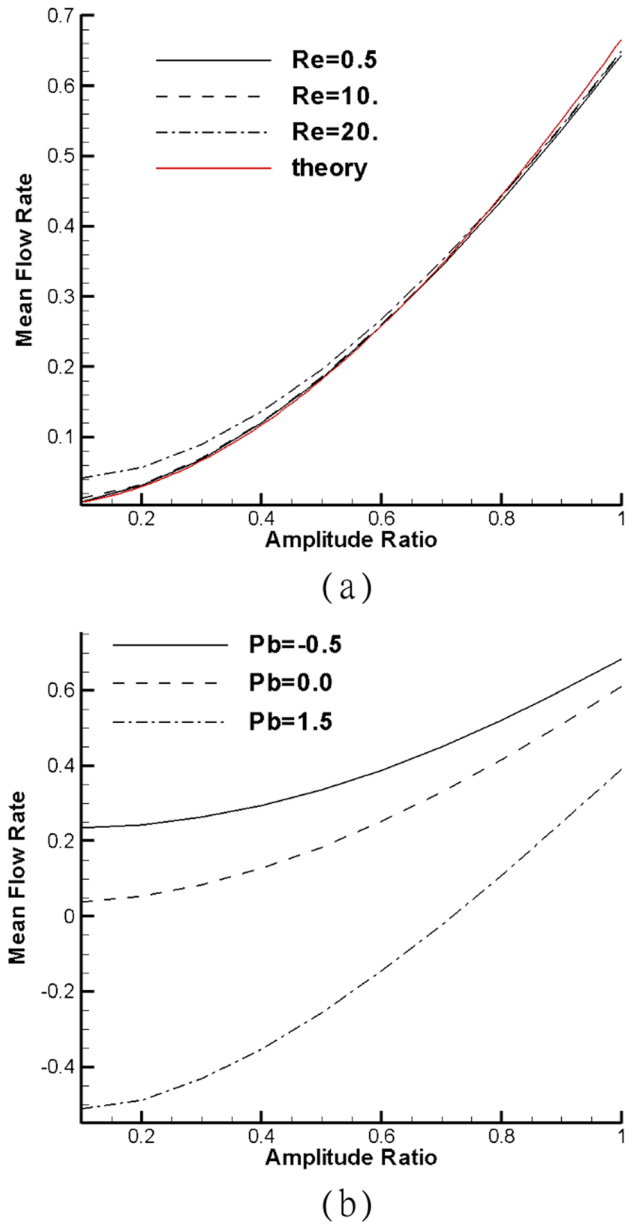

Fig. 6 Variation of mean flow rate against amplitude ratio with $\alpha = 0.0907$ for (*a*) different Reynolds numbers ($P_b = 0$) and (*b*) different back pressures (Re = 20)

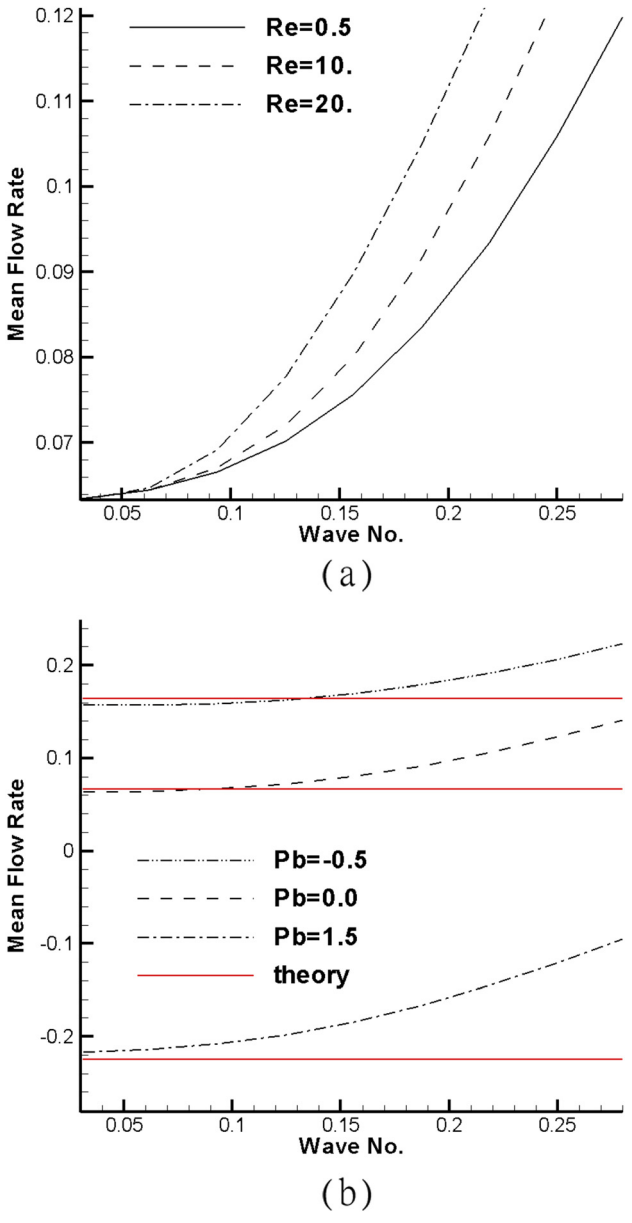

Fig. 7 Variation of mean flow rate against wave number with $\varepsilon = 0.3$ for (*a*) different Reynolds numbers ($P_b = 0$) and (*b*) different back pressures (Re = 10)

from Eq. (12). Since the wave number is, in general, not so small, this conclusion is not true, which can be verified in Figs. 7(*a*) and 7(*b*) for different Reynolds numbers and back pressures. The flow rate increases with wave number because the frequency of the peristaltic motion is increased. It can be found from the figures that the dependence of the mean flow rate on the wave number can be approximated in a parabolic manner.

3.4 Effects of Back Pressure. As seen from Figs. 8(*a*) and 8(*b*) for different wave numbers and amplitude ratios, the increase in back pressure results in a nearly linear decrease of mean flow rate, which can be identified from Eq. (12). The back pressure at which there is no mean flow can be deduced as

$$(P_b)_{\bar{Q}=0} = \frac{36L\varepsilon^2}{\mathrm{Re}(4-\varepsilon^2)^{5/2}} \tag{14}$$

The numerical values of back pressure required for zero mean flow rate are 0.37 and 1.14 for $\varepsilon = 0.3$ and 0.5, respectively, compared to the theoretical values 0.34 and 1.06. This zero-flow pressure is increased in Fig. 8(*a*) when the wave number becomes larger. However, as addressed in the above, the theory cannot tell the difference for different wave numbers.

3.5 Effects on Flow Structure. To illustrate the flow structure, streamlines at various times in a time period T for two different peristaltic amplitudes with $P_b = 1.5$, $\alpha = 0.0907$, and $\mathrm{Re} = 20$ are presented in Figs. 9 and 10. The flow fields are shown in both the laboratory and wave frames of reference. The transformation of velocity field from laboratory frame to wave frame is obtained by subtracting the wave speed c from the absolute velocity u. It is apparent that the streamline pattern in the wave frame is shaped by the walls of the channel. According to Shapiro et al. [1], flow circulation may appear in the regions under the wave crests in the wave frame when the peristaltic amplitude is large enough. However, this flow trapping phenomenon is not seen in Fig. 10 even for the case of large amplitude ratio $\varepsilon = 1.0$. The cause of this is ascribed to the channel geometry. The lower wall is motionless

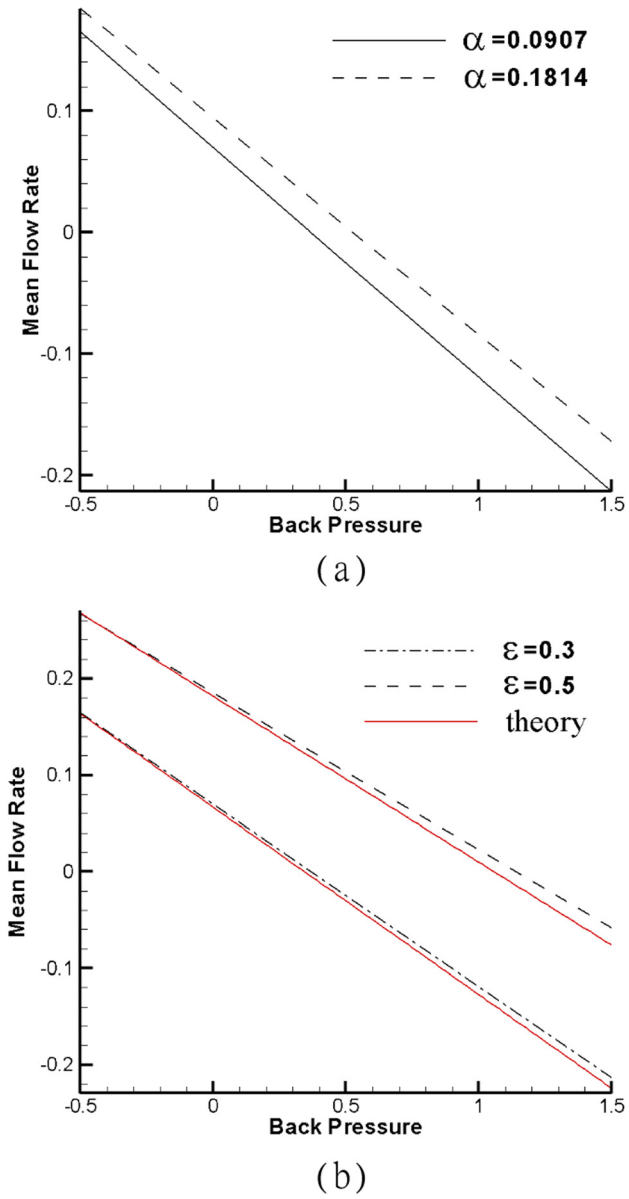

Fig. 8 Variation of mean flow rate against back pressure with Re = 10 for (*a*) two wave numbers ($\varepsilon = 0.3$) and (*b*) two amplitude ratios ($\alpha = 0.0907$)

and only the upper wall is in motion in the present study, whereas both the walls oscillate in a symmetric manner in Shapiro's study. Thus, it can be understood that there is not enough room, and thus no adverse pressure gradients large enough for the recirculating flow to develop in the crest region in this asymmetric channel. The flow field in the laboratory frame is much more complicated. As seen in Fig. 9(*b*) for the case $\varepsilon = 0.3$, a thorough stream is directed toward the inlet (the left boundary) in the region near the lower wall due to the adverse pressure gradient imposed. Isolated flow is formed in the region under each trough of the upper wall. These bolus-like zones are transported forward toward the outlet (the right boundary) by the peristalsis of the wall despite the backward flow in the boluses and the underneath stream. The through stream disappears when the amplitude of the wave is increased to $\varepsilon = 1.0$. As seen from Fig. 10(*b*), the flow in the entire channel is separated into a number of isolated zones. In the regions under the crests of the wavy wall, the flow is directed forward while in those under the troughs, the flow is in the backward direction. All these boluses move downward with the peristaltic wall. The resulting mean flow rate is positive with $\bar{Q} = 0.39$.

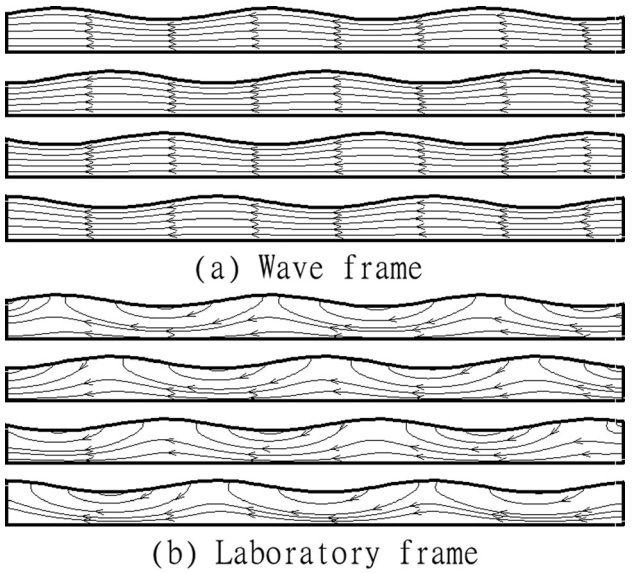

Fig. 9 Streamlines at times $t = 0$, $T/4$, $T/2$, and $3T/4$ in a time period for $\varepsilon = 0.3$ (*a*) in wave frame and (*b*) in laboratory frame ($\alpha = 0.0907$, Re = 20, and $P_b = 1.5$)

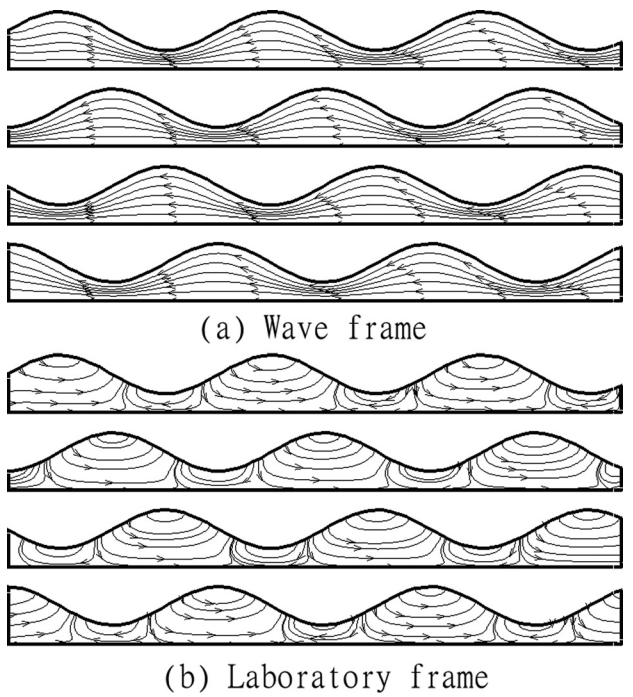

Fig. 10 Streamlines at times $t = 0$, $T/4$, $T/2$, and $3T/4$ in a time period for $\varepsilon = 1$ (*a*) in wave frame and (*b*) in laboratory frame ($\alpha = 0.0907$, Re = 20, and $P_b = 1.5$)

The instantaneous pressure variation along the lower wall for the two amplitudes is given in Fig. 11. The periodic shape of the channel results in wavy variation of pressure with a maximum in the crest region and a minimum in the trough region. Also shown is the time-mean pressure, obtained by averaging over a time period. Obviously, the mean pressure varies in a linear fashion throughout the entire channel. The wavy variation of the instantaneous pressure is superimposed on the linear mean pressure profile. As expected, the amplitude of the pressure variation increases with the amplitude of the wavy wall due to the enlarged variation of the channel height. Figure 12 presents the pressure distribution for two wave numbers

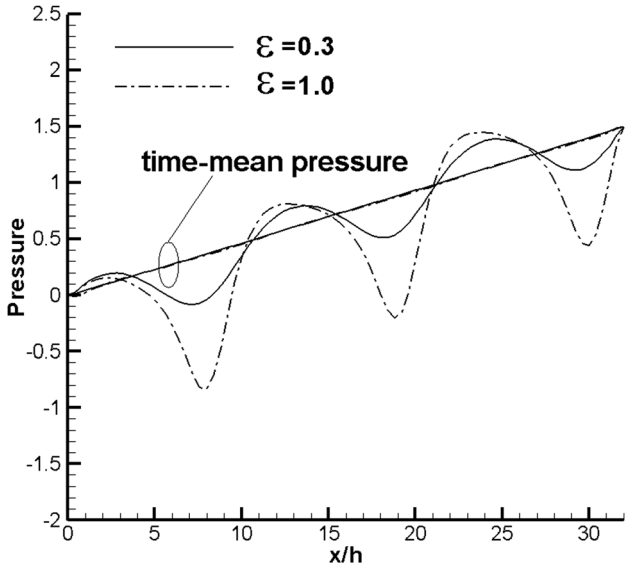

Fig. 11 Variation of pressure at the fixed wall for two amplitude ratios ($\alpha = 0.0907$, Re = 20, and $P_b = 1.5$)

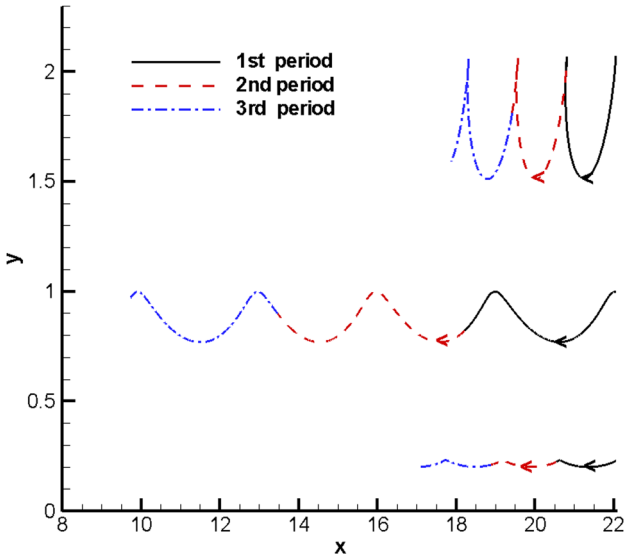

Fig. 13 Path lines for three particles ($\varepsilon = 0.3$)

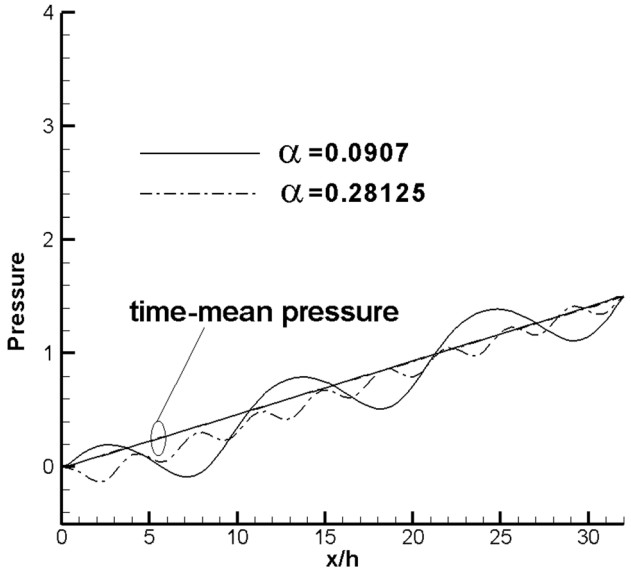

Fig. 12 Variation of pressure at the fixed wall for two wave numbers ($\varepsilon = 0.3$, Re = 20, and $P_b = 1.5$)

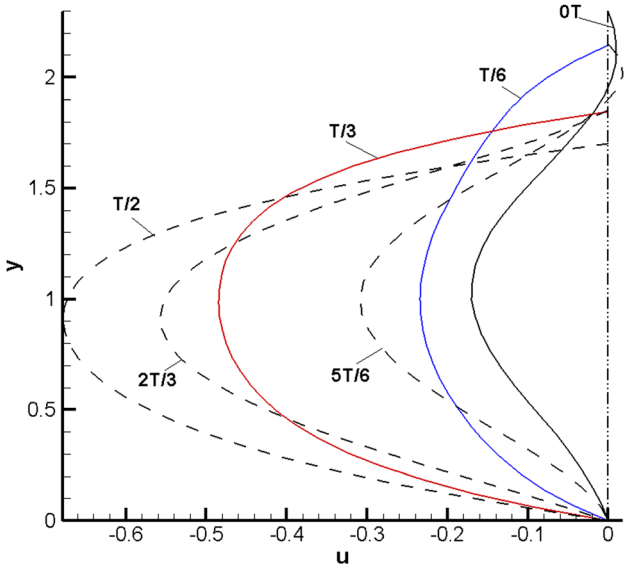

Fig. 14 Velocity profiles along a vertical line in a time period ($\varepsilon = 0.3$)

$\alpha = 0.0907$ and 0.28125 with $\varepsilon = 0.3$. Since the wavelength decreases as the wave number increases, it causes smaller variation of pressure in each wavelength as seen in the figure. The variation of pressure is also affected by Reynolds number. In general, the amplitude of the variation decreases as the Reynolds number increases.

The flow peristalsis becomes even clearer by tracing particles released in the channel. In Fig. 13, corresponding to the low amplitude case ($\varepsilon = 0.3$) given in Fig. 9, three particles are initially placed at locations $x = 22.05$ and $y = 2.007$, 1.0, and 0.23. These particles move in the backward direction in a wavy form. The closer the particle to the upper wall, the larger the oscillation amplitude. As revealed in Fig. 14, the flow is mainly in the negative direction due to the adverse pressure gradient. The velocity in the channel is higher in the core region than those near the walls. Thus, the particle initially at $y = 1.0$ travels much farther than the two near the walls. In the plot, each individual period of the peristaltic motion is marked by different line pattern. It is interesting to note that the traveling distances in individual periods are different. When the amplitude is greatly increased to $\varepsilon = 1$, loops are visible in the path lines as shown in Fig. 15 for the particles initially located at $x = 11.025$. It was seen from Fig. 10 that the boluses under the crests and the troughs are of different flow directions. The velocity profiles along the vertical axis at selected times in a time period are illustrated in Fig. 16. In the early stages of $t = 0$ and $T/6$, the flow is in the positive direction. The flow direction is reversed at the following times $t = T/3$ and $T/2$. At $t = 2T/3$, positive velocity is recovered in the region near the upper wall. It is followed by the flow becoming fully positive. Due to this kind of flow pattern, it results in loops in the path lines. In general, the particles move in the direction toward the outlet despite the looping flow, resulting in positive mean flow rate.

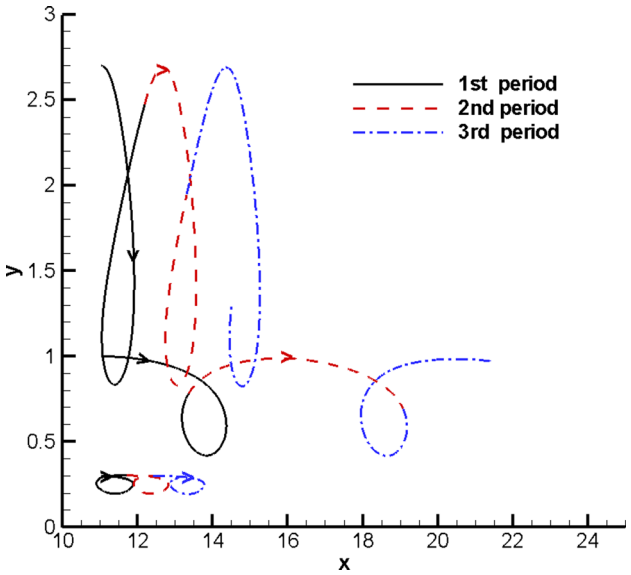

Fig. 15 Path lines for three particles ($\varepsilon = 1$)

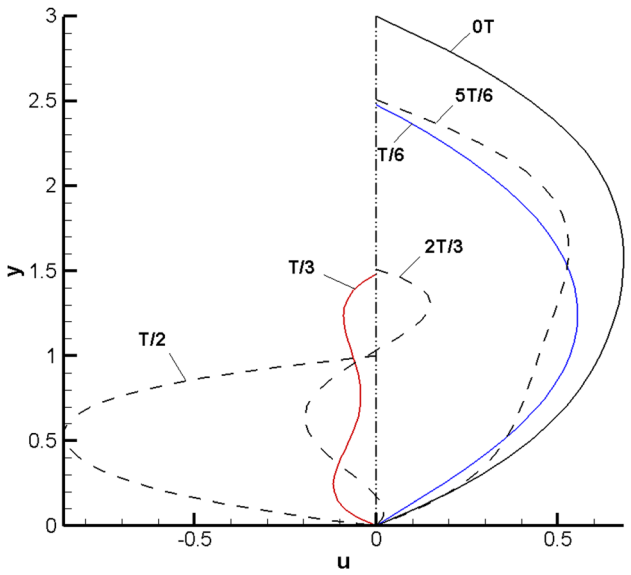

Fig. 16 Velocity profiles along a vertical line in a time period ($\varepsilon = 1$)

4 Conclusions

A numerical model based on the finite volume method has been developed to investigate the flow characteristics of peristaltic pumping in a channel. It incorporates moving-grid formulations and unstructured-grid techniques to cope with the time-dependent domain caused by peristalsis of the flexible wall. It was shown that bolus-like zones are formed in the regions under the troughs and crests of the sinusoidal wall. These boluses are transported by the peristalsis of the wall. Due to the peristaltic flow, the path lines of particles exhibit a wavy pattern. At large vibration amplitudes, flow directions in the boluses are not the same in the crest regions and trough regions, resulting in loops in the particle path. The wavy geometry of the channel causes wavy variation of pressure, which is superimposed on the linear mean pressure gradient resulting from the prescribed pressure boundary conditions. Comparison of flow rate was made between numerical simulations and lubrication model. In this model, it is assumed that both the wave number and Reynolds number are extremely small. This leads to independence of the mean flow rate on wave number and a linear relationship between flow rate and Reynolds number. It was revealed in our computational results that the flow rate increases with the wave number in a parabolic form. The theory is appropriate only when the wave number is less than 0.1 and the Reynolds number is less than 20.

Acknowledgment

The long-term financial support of the National Science Council, R. O. C., is acknowledged.

Appendix

In the wave frame of reference, which moves at speed c relative to the laboratory frame, the flow becomes steady. The transformation between the two frames is given by

$$x = X - ct, \quad u = U - c \tag{A1}$$

where u is the velocity in the x-direction in the moving frame. With the assumptions of infinite wavelength and inertia-free flow, the Navier-Stokes equations in the x-direction reduce to

$$\frac{dp}{dx} = \mu \frac{\partial^2 u}{\partial y^2} \tag{A2}$$

The coordinate of the wavy wall in the wave frame is

$$y_1(x) = 2h + a\cos\frac{2\pi x}{\lambda} \tag{A3}$$

The problem is subject to the following boundary conditions:

$$u(y = 0) = -c, \quad u(y = y_1) = -c \tag{A4}$$

The solution obtained is

$$u = \frac{(y^2 - y_1 y)}{2\mu}\frac{dp}{dx} - c \tag{A5}$$

The flow rate in the wave frame can be obtained,

$$q = \int_0^{y_1} u dy = \frac{-y_1^3}{12\mu}\frac{dp}{dx} - cy_1 \tag{A6}$$

It is noted that although each term on the right-hand side of the expression depends on the coordinate x, the flow rate itself is constant because of the steady state in the wave frame. The flow rate in the laboratory frame becomes

$$Q = \int_0^{y_1} (u + c) dy = q + cy_1 \tag{A7}$$

The time-mean flow rate is obtained by integrating over a period T

$$\bar{Q} = \frac{1}{T}\int_0^T Q dt = q + 2ch \tag{A8}$$

Equation (A6) can be rearranged to give pressure gradient in terms of flow rate

$$\frac{dp}{dx} = -12\mu\left(\frac{q}{y_1^3} + \frac{c}{y_1^2}\right) \tag{A9}$$

Substituting y_1 from Eq. (A3) and integrating this equation over a wavelength lead to the pressure rise per wavelength,

$$\Delta p_\lambda = \frac{-6\mu\lambda(8h^2 + a^2)q}{(4h^2 - a^2)^{5/2}} - \frac{24\mu ch\lambda}{(4h^2 - a^2)^{3/2}} \tag{A10}$$

In the above integration, the following formulas are used:

$$\int_0^{2\pi} \frac{d\theta}{(\alpha + \beta\cos\theta)^2} = \frac{2\pi\alpha}{(\alpha^2 - \beta^2)^{3/2}} \tag{A11a}$$

$$\int_0^{2\pi} \frac{d\theta}{(\alpha + \beta\cos\theta)^3} = \frac{\pi(2\alpha^2 + \beta^2)}{(\alpha^2 - \beta^2)^{5/2}} \tag{A11b}$$

Substituting q from Eq. (A8) and introducing dimensionless variables, Eq. (A10) yields

$$\bar{Q}^* = 2 - \frac{4(4 - \varepsilon^2)}{(8 + \varepsilon^2)} - \frac{\mathrm{Re}}{6}\frac{(4 - \varepsilon^2)^{5/2}}{(8 + \varepsilon^2)}\frac{\Delta p_\lambda^*}{\lambda^*} \tag{A12}$$

where $\bar{Q}^* = \bar{Q}/ch$, $\varepsilon = a/h$, $\mathrm{Re} = \rho ch/\mu$, $\Delta p_\lambda^* = \Delta p_\lambda/\rho c^2$, and $\lambda^* = \lambda/h$.

References

[1] Shapiro, A. H., Jaffrin, M. Y., and Weinberg, S. L., 1969, "Peristaltic Pumping With Long Wavelengths at Low Reynolds Number," J. Fluid Mech., **37**, pp. 799–825.

[2] Weinberg, S. L., Eckstein, E. C., and Shapiro, A. H., 1971, "An Experimental Study of Peristaltic Pumping," J. Fluid Mech., **49**, pp. 461–479.

[3] Mishra, M., and Rao, A. R., 2003, "Peristaltic Transport of a Newtonian Fluid in an Asymmetric Channel," Z. Angew. Math. Phys., **54**, pp. 532–550.

[4] Hayat, T., and Ali, N., 2008, "Effect of Variable Viscosity on the Peristaltic Transport of a Newtonian Fluid in an Asymmetric Channel," Appl. Math. Modelling, **32**, pp. 761–774.

[5] Reddy, M. V. S., Mishra, M., Sreenadh, S., and Rao, A. R., 2005, "Influence of Lateral Walls on Peristaltic Flow in a Rectangular Duct," ASME J. Fluids Eng., **127**, pp. 824–827.

[6] Ravi Kumar, Y. V. K., Krishna, S. V. H. N., Ramana Murthy, M. V., and Sreenadh, S., 2010, "Unsteady Peristaltic Pumping in a Finite Length Tube With Permeable Wall," ASME J. Fluids Eng., **132**, p. 101201.

[7] Srinivas, S., and Kothandapani, M., 2008, "Peristaltic Transport in an Asymmetric Channel With Heat Transfer - A Note," Int. Commun. Heat Mass Transfer, **35**, pp. 514–522.

[8] Jiménez-Lozano, J., and Sen, M., 2010, "Streamline Topologies of Two-Dimensional Peristaltic Flow and Their Bifurcations," Chem. Eng. Process., **49**, pp. 704–715.

[9] Misra, J. C., and Pandey, S. K., 2002, "Peristaltic Transport of Blood in Small Vessels: Study of a Mathematical Model," Comput. Math. Appl., **43**, pp. 1183–1193.

[10] Misra, J. C., and Maiti, S., 2012, "Peristaltic Pumping of Blood through Small Vessels of Varying Cross-Section," ASME J. Appl. Mech., **79**, p. 061003.

[11] Rao, A. R., and Mishra, M., 2004, "Peristaltic Transport of a Power-Law Fluid in a Porous Tube," J. Non-Newtonian Fluid Mech., **121**, pp. 163–174.

[12] Ravi Kumar, Y. V. K., Krishna Kumari P., Ramana Murthy, M. V., and Sreenadh, S., 2011, "Peristaltic Transport of a Power-Law Fluid in an Asymmetric Channel Bounded by Permeable Walls," Adv. Appl. Sci. Res., **2**, pp. 396–406. Available at http://www.pelagiaresearchlibrary.com/advances-in-applied-science/vol2-iss3/AASR-2011-2-3-396-406.pdf

[13] Nadeem, S., Akram, S., Hayat, T., and Hendi, A. A., 2012, "Peristaltic Flow of a Carreau Fluid in a Rectangular Duct," ASME J. Fluids Eng., **134**, p. 041201.

[14] Noreen, S., Alsaedi, A., and Hayat, T., 2012, "Peristaltic Flow of Pseudoplastic Fluid in an Asymmetric Channel," ASME J. Appl. Mech., **79**, p. 054501.

[15] Ali, N., and Hayat, T., 2008, "Peristaltic Flow of a Micropolar Fluid in an Asymmetric Channel," Comput. Math. Appl., **55**, pp. 589–608.

[16] Tripathi, D., 2011, "Numerical Study on Creeping Flow of Burgers' Fluids Through a Peristaltic Tube," ASME J. Fluids Eng., **133**, p. 121104.

[17] Fung, Y. C., and Yih, C. S., 1968, "Peristaltic Transport," ASME J. Appl. Mech., **45**, pp. 669–675.

[18] Yin, F. C. P., and Fung, Y. C., 1971, "Comparison of Theory and Experiment in Peristaltic Transport," J. Fluid Mech., **47**, pp. 93–112.

[19] Wilson, D. E., and Panton, R. L., 1979, "Peristaltic Transport due to Finite Amplitude Bending and Contraction Waves," J. Fluid Mech., **90**, pp. 145–159.

[20] Selverov, K. P., and Stone, H. A., 2001, "Peristaltically Driven Channel Flows With Applications Toward Micromixing," Phys. Fluids, **13**, pp. 1837–1859.

[21] Yi, M., Bau, H. H., and Hu, H., 2002, "Peristaltically Induced Motion in a Closed Cavity With Two Vibrating Walls," Phys. Fluids, **14**, pp. 184–197.

[22] Abd Elnaby, M. A., and Haroun, M. H., 2008, "A New Model for Study the Effect of Wall Properties on Peristaltic Transport of a Viscous Fluid," Commun. Nonlinear Sci. Numer. Simul., **13**, pp. 752–762.

[23] Usha, S., and Rao, A. R., 2000, "Effects of Curvature and Inertia on the Peristaltic Transport in a Two-Fluid System," Int. J. Eng. Sci., **38**, pp. 1355–1375.

[24] Rao, A. R., and Mishra, M., 2004, "Nonlinear and Curvature Effects on Peristaltic Flow of a Viscous Fluid in an Asymmetric Channel," Acta Mech., **168**, pp. 35–59.

[25] Brown, T. D., and Hung, T.-K., 1977, "Computational and Experimental Investigations of Two-Dimensional Nonlinear Peristaltic Flows," J. Fluid Mech., **83**, pp. 249–272.

[26] Takabatake, S., and Ayukawa, K., 1982, "Numerical Study of Two-Dimensional Peristaltic Flows," J. Fluid Mech., **122**, pp. 439–465.

[27] Tong, P., and Vawter, D., 1972, "An Analysis of Peristaltic Pumping," ASME J. Appl. Mech., **39**, pp. 857–862.

[28] Rathish Kumar, B. V., and Naidu, K. B., 1995, "A Numerical Study of Peristaltic Flows," Comput. Fluids, **24**, pp. 161–176.

[29] Pozrikidis, C., 1987, "A Study of Peristaltic Flow," J. Fluid Mech., **180**, pp. 515–527.

[30] Demirdzic, I., and Peric, M., 1988, "Space Conservation Law in Finite Volume Calculations of Fluid Flow," Int. J. Numer. Methods Fluids, **8**, pp. 1037–1050.

[31] Tsui, Y.-Y., and Pan, Y.-F., 2006, "A Pressure-Correction Method for Incompressible Flows Using Unstructured Meshes," Numer. Heat Transfer, Part B, **49**, pp. 43–65.

[32] Tsui, Y.-Y., and Wu, T.-C., 2010, "Use of Characteristic-Based Flux Limiters in a Pressure-Based Unstructured-Grid Algorithm Incorporating High-Resolution Schemes," Numer. Heat Transfer, Part B, **55**, pp. 14–34.

[33] Tsui, Y-Y., and Chang, T.-C., 2012, "A Novel Peristaltic Micropump With Low Compression Ratios," Int. J. Numer. Methods Fluids, **69**, pp. 1363–1376.

[34] Issa, R. I., 1986, "Solution of the Implicitly Discretised Fluid Flow Equations by Operator-Splitting," J. Comput. Phys., **62**, pp. 40–65.